

Data-driven rational approximation for composite boom deployment on a cubesat via Vector-Fitting

Deven H. Mhadgut ^{*}, Austin Phoenix[†], Jonathan Black[‡]
Virginia Polytechnic Institute and State University, Blacksburg, VA, 24060

Thin-ply composite laminates are widely used in deployable space structures for small satellites due to their low mass and high packing efficiency. However, there remains a knowledge gap in predicting the structural dynamics and the loading that these deployments have on the chassis of the satellite. As the size of deployable structures increases, this information becomes even more important for the incorporation of booms with embedded data and power into space missions. Ut ProSat-1(UPS-1), a 3U cubesat, aims to passively self-deploy a bistable composite boom on orbit. The boom experiment includes IMUs at the tip and root inside the chassis. These IMUs will measure the frequency response of the structure in terms of the 3D acceleration due to the deployment of the boom. Here, we present the results of ground tests that were designed to serve as a baseline for the on-orbit mission. To replicate the thermal effects, tests were performed in an environmental chamber under a pressure of 9 Torr and with temperature cycling from 4 to 70°C. Characterization of the satellite system parameters is necessary to validate these results and understand the effects of temperature changes on the deployments. Transfer functions were obtained from the two IMUs and then interpolated to form a low dimensional numerical model by minimizing the least square errors through the process of Vector Fitting (VF). The state-space model, thus obtained, can be used as a starting point for developing an analytical model for predicting the deployment dynamics of self-deployable booms in space.

Nomenclature

$H(s)$	= Transfer Function of original system
N_s	= Number of samples
r	= Degree of reduced-order system
λ	= Poles of the system
$\tilde{l}_i(s), \tilde{l}(s)$	= Nodal polynomials
ϕ, ψ	= Approximation parameters
$\tilde{H}(s)$	= Transfer Function of approximate system
α, β	= Real, Imaginary parts of the system poles
Subscripts	
i	= Frequency index
Superscripts	
k	= Least-Squares iteration number

I. Introduction

Composite laminate tape spring booms have demonstrated significant potential as morphing structures, leading to their extensive use in various aerospace engineering domains over the last decade, including on-orbit deployment of spacecraft components like magnetometers and solar sails[1]. Our study focuses on environmental tests designed to quantify the deployment dynamics of a parabolic tape spring boom. The boom specimen utilized in the tests was produced at NASA Langley, and an identical boom will be deployed aboard the Ut ProSat-1 (UPS-1)[2], a 3U

^{*}Graduate Student, Department of Aerospace and Ocean Engineering

[†]Research Associate Professor, Mission Systems Division, National Security Institute

[‡]Professor, Department of Aerospace and Ocean Engineering

CubeSat designed and built by students, faculty, and research staff at Virginia Tech. These booms are open-section composite tape-springs with a parabolic cross-section and exhibit bistability due to their unique geometry and material characteristics, making them self-deployable. The key experimental objective of UPS-1 is to demonstrate repeated self deployments of this boom with the help of an innovative deployer. In the stowed position, the deployer spool is kept in place by a shutter mechanism[3] actuated via a servo motor.

The tip of the boom includes a flexible circuit[4](shown in Fig.1) with a LSM6DSO32 6-axis MEMS inertial measurement unit (IMU). The payload control module (PCM) circuit board inside the CubeSat chassis includes three additional BMI270 6-axis MEMS IMUs (two extra for triple modular redundancy), which measure the instantaneous accelerations at these positions. The boom laminate has three plies and eight 44 AWG copper wires co-located with the central ply. These wires run along the length of the boom and enable data and power transmission to and from the boom tip. These two IMUs measure accelerations at their respective locations and represent the input and output to a black box model of the underlying dynamical system. Also, as there is no active vibration/actuation source on the satellite, the end-of-deployment acceleration measured by the boom-tip IMU is assumed to be the input to the system and the PCM IMU acceleration acts as the output. The aim of this project is to assist in a continuous effort to predict with accuracy the dynamics of the self-deploying boom and the excitation imparted to the chassis. To begin with, we performed several thermal vacuum(TVAC) deployment tests[5] with a prototype of the integrated satellite and the results from two of those have been presented here.

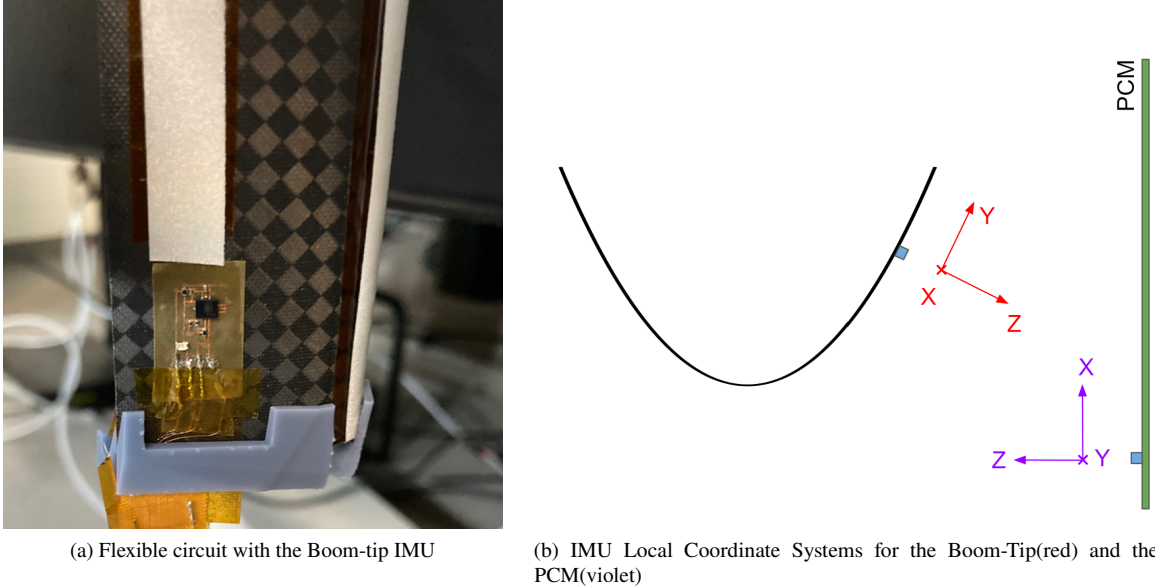


Fig. 1 IMU Configuration

The first step towards validating the results for consistency would be to use these sensor measurements to create an approximate mathematical model of the system. Over the last few decades, many techniques of "system identification" have been developed to estimate the system parameters from their frequency response functions (FRFs). These techniques enable us to identify modal properties of the test structure. One of the earliest approaches was the peak-picking method which is simply looking at the frequency domain plots and identifying the resonant peaks as the modes of the system. However, this approach works well only when the peaks are real and well separated and the damping is not too high. Ewins [6] proposed the 'circle-fitting' method which exploits the fact that transfer function points describe a circle in the Nyquist plane around the resonance of the system. This approach becomes susceptible to errors for noisy data with closely spaced peaks. Later, Maia and Silva [7] proposed defining the FRF in a rational fractional form consisting of orthogonal polynomials. Gustavsen and Semlyen [8] used this idea to develop vector-fitting (VF). This involves solving a sequence of least square fitting problems (Sanathanan-Koerner iterations [9]) with pole relocation at every step. Gustavsen [10] further improved upon this process by modifying the VF scaling function to incorporate a more relaxed criterion. Finally, Deschrijver et. al [11] presented an improvement over the original VF algorithm. This "fast" approach (used here) is based on QR decomposition and has proven to significantly reduce computation time for large scale

models. This implementation is numerically robust and can generate state-space models directly from input-output data.

As mentioned earlier, the boom under study is self-deployable and its uncontrolled deployment can have detrimental effects on any payload attached to it. Repeated deployments would even damage the internal copper wires putting any data transmission through the boom at risk. We propose a novel approach to solve this problem. We plan to use the identified state-space model to design and implement control algorithms to provide active vibration suppression at the end of each boom deployment. Piezoelectric actuators may be used to provide the necessary strains to achieve closed loop control. Le [12] showed experimentally that the Linear Quadratic Regulator (LQR) state feedback method provided the best settling time for a flexible beam model compared to the Derivative (D) and Proportional-Derivative (PD) controllers. Adel et al. [13] derived a state space model from finite-element method(FEM) and used that to test the efficiency of a Proportional-Integral-Derivative (PID) controller for vibration suppression. More recently, Aktas and Esen [14] investigated the effects of the actuator location on the damping capability of the controller. Finally, Li et al. [15] used LQR for designing active control under instantaneous and continuous disturbances. Future efforts will involve performing experiments to validate these ideas.

This paper is organized as follows: The experimental setup and test methodology are introduced in Section II. Then, the process of obtaining system information through rational approximation is presented in Section III. The results of the deployment experiments at two different temperatures and their corresponding estimates are discussed in section IV. The paper is concluded in Section V, where the plan for future work has been discussed.

II. Experimental Setup

The satellite chassis with the stowed boom was mounted inside a Tenney environmental chamber using an Aluminum extrusion rod and 3-D printed ABS plugs (as shown in Fig.2). The chassis was then inclined at 30°with the horizontal to allow for full deployment of the 4-ft long boom in the chamber. The temperature at the two IMU sensor locations were monitored using two infrared (IR) cameras mounted on the chamber walls. This temperature data was recorded using a Teensy 4.1 microcontroller board. This helped ensure that the temperature displayed on the chamber controller screen matched the temperature reached on the satellite.

The boom was deployed passively by unlocking the spool using the servo motor. This was done multiple times to resemble the on-orbit experiments. The IMU data was collected for a period of 10 seconds from the start of deployment and then transmitted in packets from the boom-tip circuit to the PCM board where it is processed and stored in a microSD card. The IMU provides three axis acceleration data for analysis. The next step was to align the local coordinate systems of the two IMUs. In this case, the PCM coordinate system was transformed into the boom-tip IMU system. It is worth noting that the boom is flexible and the parabolic profile and the associated coordinate system changes as the boom deploys. However, as the area of focus here, is the end-of-deployment regime, only the final state of the boom-tip IMU coordinate system was considered for the transformation. The components of the gravity vector are then subtracted from these results. This needs to be done as the IMUs give a 1G reading at rest.

III. Rational approximation using Vector Fitting

The mathematical procedure for generating the state-space model (rational approximation) from experimental FRF measurements is described here. Also, although the system in consideration is single-input single-output (SISO), this method is applicable for other types of systems [16].

As mentioned earlier, the boom-tip IMU sensor is considered to be the excitation force or the input (denoted by x) and the PCM IMU measurements are the outputs (y) to the underlying dynamical system. The acceleration values obtained from the two sensors are first converted from the time domain to the frequency domain using the Fast Fourier Transform (FFT). The input and output frequency series values(denoted by X and Y respectively), thus obtained, can be used to give us the true transfer function, $H(s) = Y(s)/X(s)$, for each frequency s . However, our system is nonlinear and time-variant. Therefore, it is not possible to obtain the true transfer function due to the presence of measurement noise. However, its is possible to estimate H at any frequency $s = i\omega$ using the \hat{H}_1 and \hat{H}_2 estimators given by:

$$\begin{aligned}\hat{H}_1(i\omega) &= \frac{\hat{S}_{yx}(i\omega)}{\hat{S}_{xx}(i\omega)} \\ \hat{H}_2(i\omega) &= \frac{\hat{S}_{yy}(i\omega)}{\hat{S}_{yx}(i\omega)}\end{aligned}$$

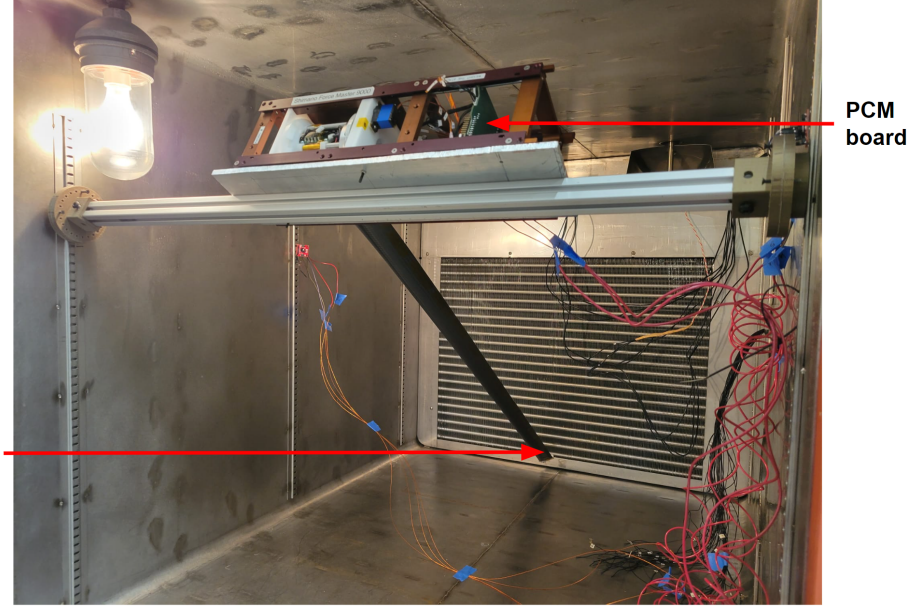


Fig. 2 Experimental setup and fully-deployed boom inside the TVAC chamber

where, $\hat{S}_{yx}(i\omega) = E[Y(i\omega)X(i\omega)^*]$ denotes the estimate of the cross-spectral density (CSD) of y and x and $\hat{S}_{xx}(i\omega) = E[X(i\omega)X(i\omega)^*]$ and $\hat{S}_{yy}(i\omega) = E[Y(i\omega)Y(i\omega)^*]$ are the estimates of the power/auto spectral density (PSD) of x and y respectively. These were calculated in Matlab using Welch's method. In the absence of noise, $\hat{H}_1(i\omega)$ and $\hat{H}_2(i\omega)$ result in identical FRFs. However, they are quite different in the presence of noise in either the input or the output measurements. The quality of the measured FRFs can be determined by the coherence function $\gamma^2(i\omega)$ which is defined as the ratio of the two estimators i.e. $\gamma^2(i\omega) = \hat{H}_1(i\omega)/\hat{H}_2(i\omega)$. Here, we only consider $\hat{H}_1(i\omega)$ and refer to it as $H(i\omega)$.

Therefore, the starting point here is a set of transfer functions evaluated for the frequency range of interest, denoted by $H(s_1), H(s_2), \dots, H(s_{N_s})$ where N_s is the number of samples and frequencies, $s_i = (i\omega_i)$. The final aim here is to construct a degree- r rational approximant (transfer function), $\tilde{H}(s) = \tilde{C}(sI - \tilde{A})^{-1}\tilde{B}$ that is able to fit the collected data in a satisfactory manner. The degree- r here is the degree of approximation which determines the size of the reduced state-space model.

Let $n(s) = \alpha_0 + \alpha_1 s + \dots + \alpha_{r-1} s^{r-1}$ and $d(s) = \beta_0 + \beta_1 s + \dots + \beta_{r-1} s^{r-1} + s^r$ denote the numerator and denominator of the rational function, respectively, i.e.,

$$\tilde{H}(s) = \frac{n(s)}{d(s)} = \frac{\alpha_0 + \alpha_1 s + \dots + \alpha_{r-1} s^{r-1}}{\beta_0 + \beta_1 s + \dots + \beta_{r-1} s^{r-1} + s^r} \quad (1)$$

where the numerator($n(s)$) and the denominator($d(s)$) are degree- $(r-1)$ and degree- r polynomials respectively. This is done to have a strictly proper rational function for the problem presented in this paper. This is not a restriction and the problem can be solved without this condition as well. The coefficients α_i and β_i are evaluated using the least-squares method. As this formulation is based on the method proposed by Gustavsen, $\tilde{H}(s)$ is calculated such that the weighted LS error (ε_{LS}) is minimized i.e.,

$$\varepsilon_{LS} = \sum_{i=1}^{N_s} w_i |H(s_i) - \tilde{H}(s_i)|^2 = \sum_{i=1}^{N_s} w_i \left| H(s_i) - \frac{n(s_i)}{d(s_i)} \right|^2 \rightarrow \min. \quad (2)$$

It is to be noted that the unknown coefficients in equation 1 appear in both the numerator and denominator. Therefore, the minimization problem is a nonlinear least-squares (LS) problem and can be linearized by ignoring the denominator in this expression to get a linear LS problem, such that

$$\varepsilon_{LS}^{lin} = \sum_{i=1}^{N_s} w_i |d(s_i)H(s_i) - n(s_i)|^2 \quad (3)$$

Alternatively, it can also be solved in an iterative manner based on the relaxed scheme proposed by Sanathanan and Koerner (SK iteration [9]). The algorithm is based on solving a sequence of LS problems where instead of ignoring the denominator, it is replaced by the denominator from the previous step. At the k^{th} step, the LS error is minimized by solving for $n^{(k+1)}(s)$ and $d^{(k+1)}(s)$ in equation4

$$\sum_{k=1}^{N_s} w_i \left| \frac{d^{(k+1)}(s_i)H(s_i) - n^{(k+1)}(s_i)}{d^{(k)}(s_i)} \right|^2 \rightarrow \min. \quad (4)$$

The VF method is an improvement over the SK iteration and uses the barycentric representation of $\tilde{H}(s)$ shown in equation. This parameterization is done by assuming $\tilde{H}(s) = \frac{p_r(s)}{q_r(s)}$. Then, ($r+1$) mutually distinct poles, $(\lambda_1, \lambda_2, \dots, \lambda_{r+1})$ are picked and the following nodal polynomials are defined.

$$\tilde{l}_i(s) = \prod_{\substack{k=1 \\ k \neq i}}^{r+1} (s - \lambda_k); \tilde{l}(s) = \prod_{k=1}^{r+1} (s - \lambda_k) \quad (5)$$

Now, we can define $\tilde{H}(s)$ as follows:

$$\tilde{H}(s) = \frac{p_r(s)}{q_r(s)} = \frac{\sum_{i=1}^{r+1} \phi_i \frac{\tilde{l}_i(s)}{\tilde{l}(s)}}{\sum_{i=1}^{r+1} \psi_i \frac{\tilde{l}_i(s)}{\tilde{l}(s)}} = \frac{\sum_{i=1}^{r+1} \frac{\phi_i}{s - \lambda_i}}{\sum_{i=1}^{r+1} \frac{\psi_i}{s - \lambda_i}} \quad (6)$$

This can be rewritten in a discretized form as:

$$\tilde{H}^{(k)}(s) = \frac{\tilde{n}^{(k)}(s)}{\tilde{d}^{(k)}(s)} = \frac{\sum_{i=1}^r \frac{\phi_i^{(k)}}{(s - \lambda_i^{(k)})}}{1 + \sum_{i=1}^r \frac{\psi_i^{(k)}}{(s - \lambda_i^{(k)})}} \quad (7)$$

where $\phi_i^{(k)}, \psi_i^{(k)}, \lambda_i^{(k)} \in \mathbb{C}$.

As in the SK iteration, this is now a linear LS problem and can be solved by an iteration scheme based on pole relocation. The iteration runs for 50 steps until sufficient convergence of the poles. The final rational approximation is given by

$$\tilde{H}(s) = \sum_{i=1}^r \frac{\phi_i}{s - \lambda_i} = \tilde{\mathbf{C}}(s\mathbf{I} - \tilde{\mathbf{A}})^{-1}\tilde{\mathbf{B}}. \quad (8)$$

Therefore, the experimental FRF results were used to develop a state space model for the cubesat-boom system. In this case, a set of 4001 samples was fitted to a reduced order linear system and the state matrices $[\tilde{A}, \tilde{B}, \tilde{C}, \tilde{D}, \tilde{E}]$ were obtained via the "Fast, Relaxed Vector Fitting(FRVF)" implementation in Matlab. It was observed by Albakri et al ([17],[18]), that fitting the FRFs directly on the full spectrum was prone to errors due to its sensitivity to initial poles selection. Also, the frequency spacing between resonant frequencies for complex models, like the one under study, is non-uniform.

To tackle this problem, the full frequency spectrum of around 200 Hz was divided into 32 smaller bands of 64 samples each. This allows for smaller approximation orders per band and greater accuracy of the fit. Also, the boom has a "bounce back" at the end of deployment. This might induce some rigid-body modes leading to added inaccuracies due to numerical instabilities at 0 Hz. To prevent this, the 0 Hz poles were removed from the present analysis. The poles for the smaller bands are initialized as complex-conjugate pairs such that the n^{th} pair of poles is of the form $p^{2n-1} = -\alpha + i\beta, p^{2n} = -\alpha - i\beta$ as suggested by Gustavsen [8]. Here, the imaginary part β indicates the oscillatory behavior and the real part ($\alpha = \beta/100$) represents the damping characteristic of the dynamical system. The smaller frequency bands are sequentially fitted and the updates poles from the VF algorithm are recorded. These resulting poles are used to initialize the VF process for the full spectrum and the results of the fit have been presented in the next section.

As discussed earlier, the VF algorithm is based on minimizing the L_2 (squared) error and therefore is more accurate in capturing high-valued data-points. As a result, the VF-fits are better at the resonant frequencies compared to the anti-resonant frequencies. This issue can be addressed by using different weighting methods for calculating the least

squares cost function in Eqn.2. In this work, four weighting functions are considered: unit weight ($w_j=1$), coherence ($\gamma^2(i\omega_j)$), weak inverse function ($w_j(i\omega_j) = 1/\sqrt{|H(i\omega_j)|}$) and a hybrid function ($w_j(i\omega_j) = \gamma^2(i\omega_j)/\sqrt{|H(i\omega_j)|}$). The unit weight and the weak inverse functions have been traditionally used in the past and capture the FRFs accurately at the resonances and antiresonances respectively. Also, we know that the signal-to-noise(SNR) ratio reduces at the FRF valleys, which in turn leads to a reduction in the coherence values(as seen in Fig.3). The remaining two weighting options are based on this observation. Plotting the VF results shows that the two inverse weighting functions perform better at the valley points. It was also observed that the weak-inverse function leads to over-fitting of the results which in turn would inherently include the noise in the data. To avoid this problem, the hybrid weighting scheme was selected for fitting the full FRF.

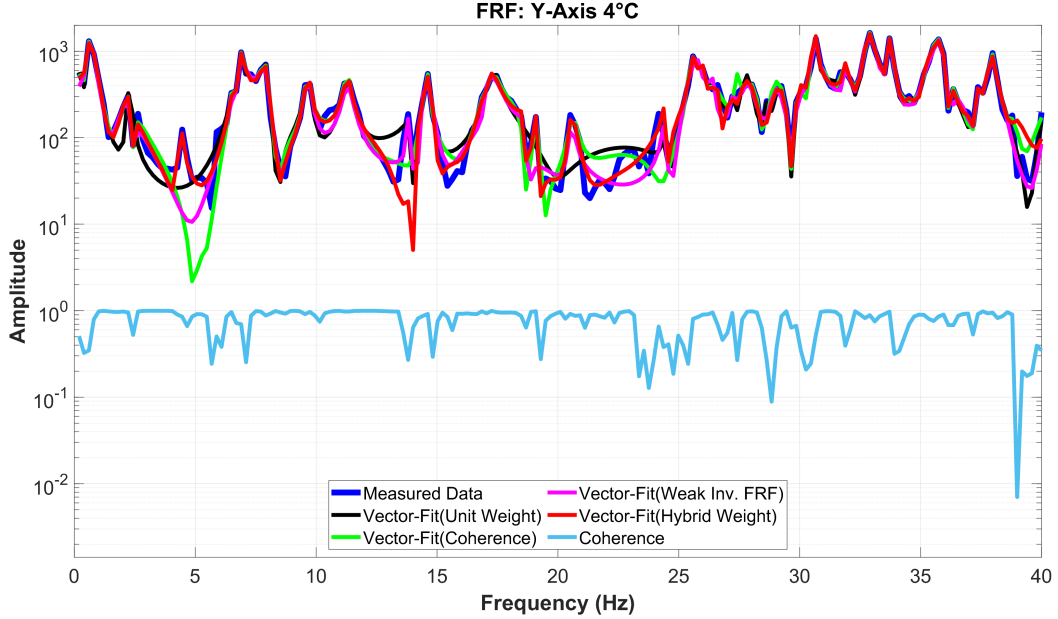


Fig. 3 Y-axis FRF compared to the VF prediction at 4°C 9 Torr and coherence for the sub-band 0-40 Hz

IV. Results and discussion

In this section, the acceleration plots in the time-domain have been presented for the boom-tip accelerometer. Similar plots are obtained for the PCM-IMU. This time-data is converted into the frequency domain and the transfer functions values are obtained between the two IMU sensors over the full spectrum. These values are used to obtain an approximate model of the system using vector-fitting. This VF fit has been plotted over the original acceleration data for deployment tests at 4°C and 70°C. The results have been shown for all three axes of the accelerometers.

Accelerometer responses are recorded and plotted against time for the 4°C and low vacuum (9 Torr) case. This time-series data was then denoised by applying the median filter to remove any visible outliers. The filtered acceleration data from the Boom-tip is shown in Fig. 4. A similar plot(not shown here) can be obtained for the 70°C case. A maximum acceleration value of around ± 40 m/s² is observed along the transverse axes(Y and Z) for the boom-tip IMU. As mentioned earlier, the boom is deployed at an angle of 30°with the horizontal. The corresponding components of gravity are subtracted from the data before plotting. The deployment can be seen in the form of chaotic accelerations of the system. It should be noted that the acceleration of the boom in the Y and Z-axes decays much slower and has the highest peaks at the end of deployment.

Next, similar plots can be obtained for the 70°C case. There is a clear shift in the frequency data between these two temperatures, confirming that temperature has a significant effect on the system properties. The input(Boom-IMU) and output acceleration(PCM-IMU) power spectral densities(PSD) have been shown in Fig.5 and Fig.6 respectively. The first mode of vibration shifted from 5.2 to 4 Hz on increasing the temperature from 4 °C to 70 °C. The decrease in the fundamental frequency of the boom might be due to the decrease in its material stiffness with the increase in

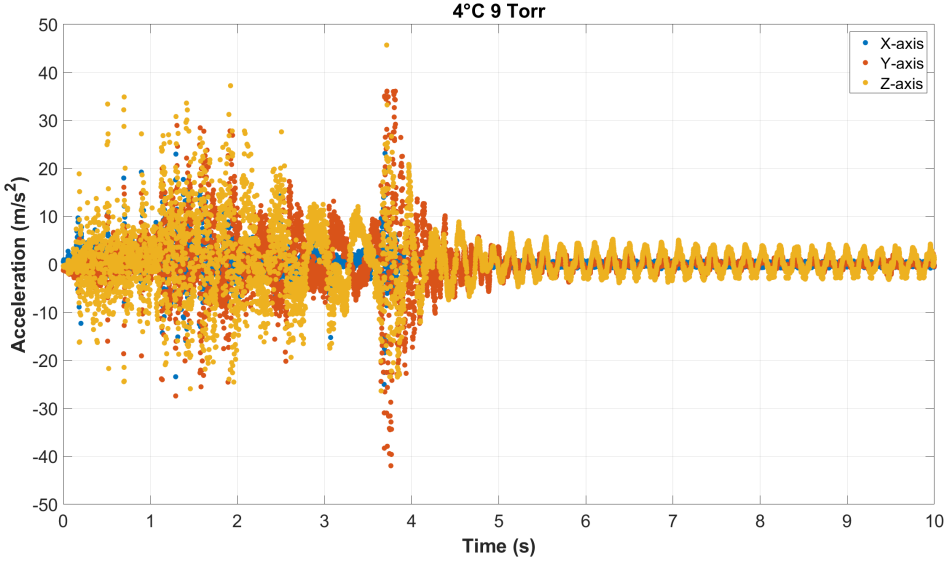


Fig. 4 Boom-Tip Acceleration

Table 1 Change in vibration modes with temperature

Test	-	Mode 1(Hz)	Mode 2(Hz)	Mode 3(Hz)
25 °C No Vac	Boom	5	10	-
	PCM	19.6	39.2	59.8
4 °C 9 Torr	Boom	5.2	12.4	-
	PCM	19	38	59.2
53°C 9 Torr	Boom	5	10	-
	PCM	19	38	59
70°C 9 Torr	Boom	4	11.6	-
	PCM	19	38	59

temperature. A similar trend can be seen for the second mode as well. The input plots also show some rigid body modes(peaks at 0 Hz) along all the three axes as a result of the boom "bounce back" behavior. This happens when the boom tries to respool itself by a small amount at the end of each deployment. On the contrary, the frequency response of the PCM IMU shows low-amplitude constant peaks for all the axes as it is rigidly fixed inside the satellite chassis.

Plots 7,8,9 show the fast relaxed vector fit (FRVF) for the three axes of 4°C case. It can be seen that the VF algorithm is able to match the resonant peaks almost perfectly for the lower frequency values up to 25 Hz. This is particularly important because the primary goal here is to obtain a data driven model that highlights the natural modes of the system. Also, it is to be noted that this is the result after 50 iterations of the VF algorithm based on the updated poles of the full frequency spectrum. As the first three modes of the boom lies within this range [5], it was decided to accept this solution. However, higher number of iterations could be considered for improved accuracy for the higher frequency data. Also, there is a considerable mismatch between the anti-peaks (troughs) for the lower frequencies. This could be rectified by increasing the number of poles used for these simulations.

Finally, the metric for convergence was chosen to be the root mean squared (RMS) error between the consecutive iterations of the VF fit. Two types of relative error definitions have been used in this paper for gauging the quality of the fit.

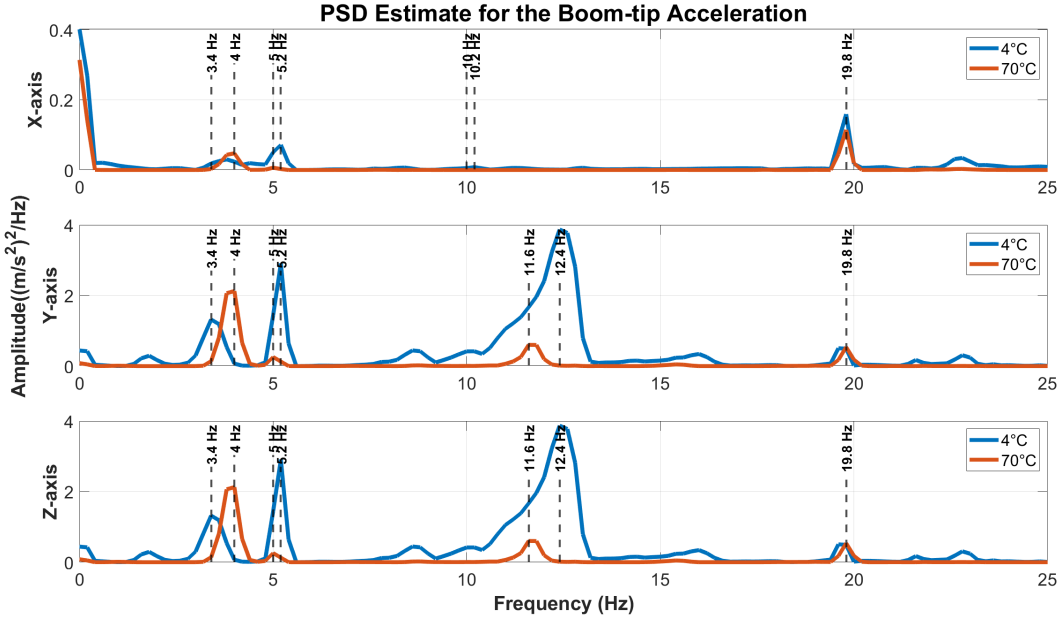


Fig. 5 Input Acceleration

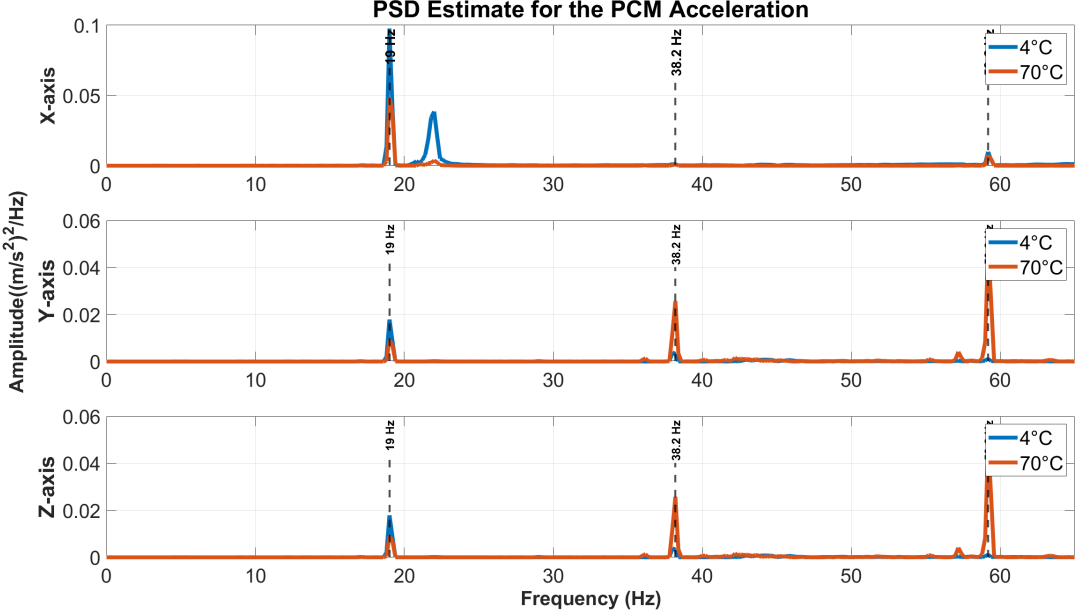


Fig. 6 Output Acceleration

$$E_{L_2} = \frac{1}{N} \sqrt{\frac{\sum_{j=1}^N \|H(i\omega_j) - \tilde{H}(i\omega_j)\|_2^2}{\sum_{j=1}^N \|H(i\omega_j)\|_2^2}} \quad \text{and} \quad E_{L_2}^w = \frac{1}{N} \sqrt{\frac{\sum_{j=1}^N w_j \|H(i\omega_j) - \tilde{H}(i\omega_j)\|_2^2}{\sum_{j=1}^N w_j \|H(i\omega_j)\|_2^2}}.$$

where E_{L_2} compares the fitted data-driven model($\tilde{H}(i\omega_j)$) and the experimental FRF data ($H(i\omega_j)$). The other error, $E_{L_2}^w$ takes the effect of the different weighting schemes(w_j) into account. The values of E_{L_2} for all the axes for the 4°C case have been presented in Table 2. It can be observed that the maximum error seen was around 1.86×10^{-4} along the Y-axis. Also, even though the hybrid weighting function does not give the minimum errors, it is able to capture the

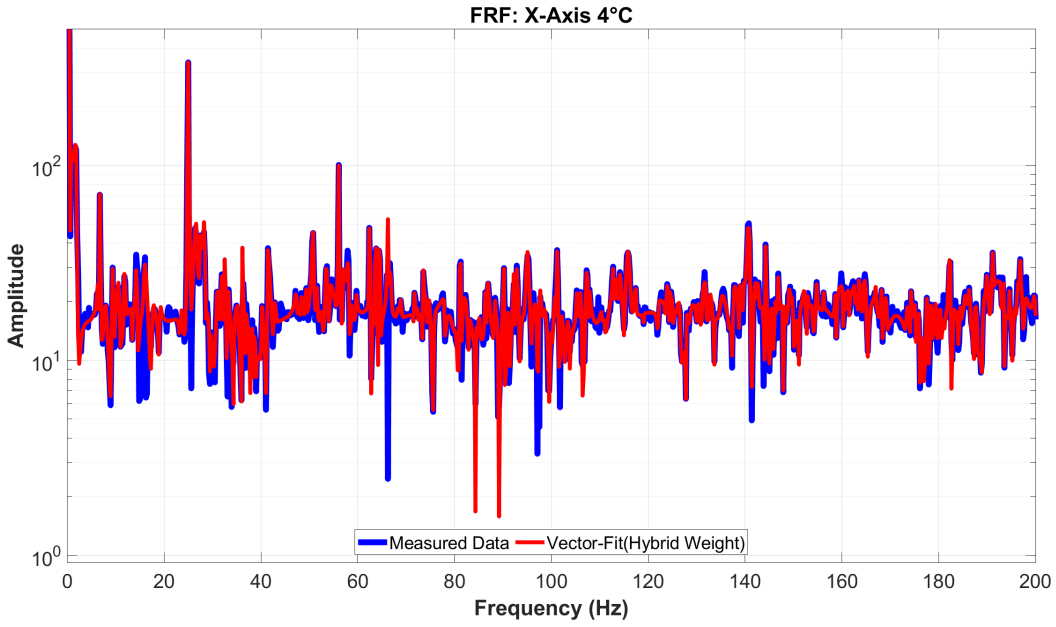


Fig. 7 X-axis FRF compared to the VF prediction at 4°C 9 Torr

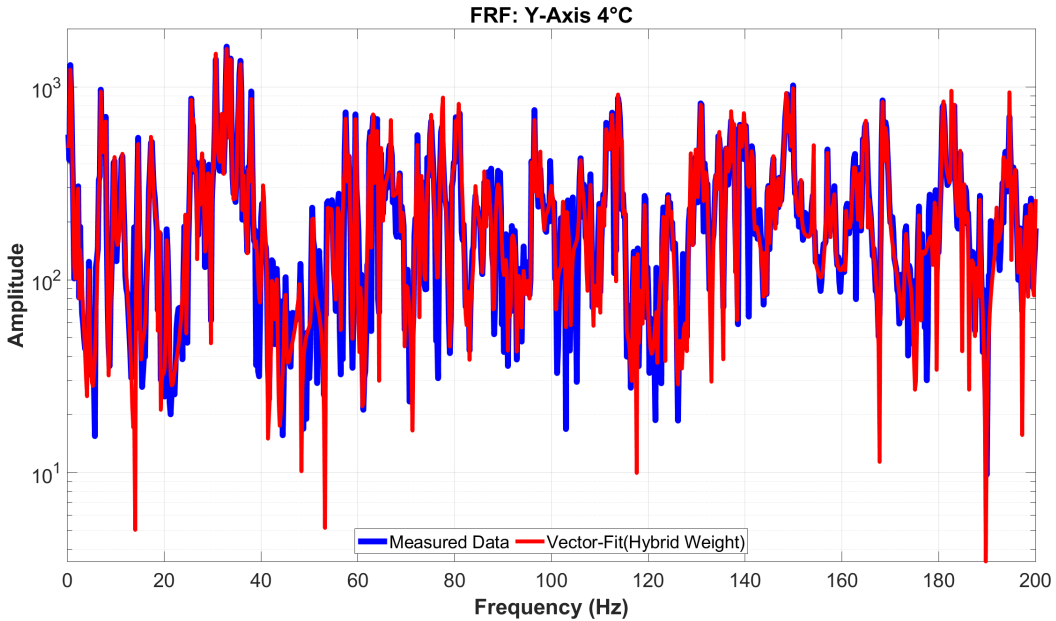


Fig. 8 Y-axis FRF compared to the VF prediction at 4°C 9 Torr

anti-peaks better than the rest of the functions as seen from the Y-axis vector-fitting prediction(Fig.3).

There are multiple reasons for the errors. First of all, the IMU was selected due to its size and weight resulting in noisy data with limited bandwidth and sensitivity. This means that the VF algorithm tries to fit the noise along with the resonant peaks. Secondly, the sampling rates are low leading to a reduced capacity to eliminate the noise from this data. Also, the actuation force is not a perfect impulse due to the boom root bouncing back and forth by a small amount at the end of each deployment. Finally the TVAC chamber was operating during testing resulting in additional noise in the signal. Future efforts will involve designing better experiments and data processing to reduce the noise.

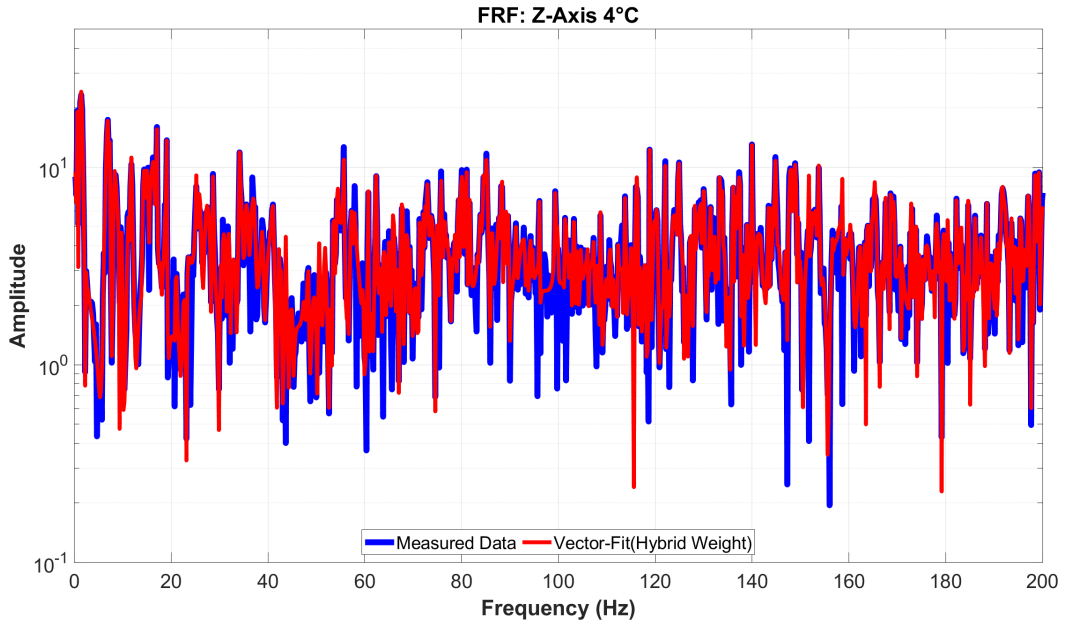


Fig. 9 Z-axis FRF compared to the VF prediction at 4°C 9 Torr

Table 2 Performance of VF algorithm in fitting weighted experimental FRFs

Weighting function (w_j)		$E_{L_2}(X)$	$E_{L_2}(Y)$	$E_{L_2}(Z)$
Unit weight	$w_j = 1$	2.96×10^{-5}	9.59×10^{-5}	7.92×10^{-5}
Coherence	$w_j = \gamma^2(i\omega_j)$	3.61×10^{-5}	1.62×10^{-4}	1.48×10^{-4}
Weak inv. FRF	$w_j = \frac{1}{\sqrt{H(i\omega_j)}}$	2.22×10^{-5}	1.25×10^{-4}	9.03×10^{-5}
Hybrid weight	$w_j = \frac{\gamma^2(i\omega_j)}{\sqrt{H(i\omega_j)}}$	4.66×10^{-5}	1.86×10^{-4}	1.43×10^{-4}

V. Conclusion and Future Work

Thermal vacuum tests were performed on the novel self-deployable "smart" boom with embedded copper traces. The deployment dynamics of the specimen were investigated, and the results were documented. It was observed that there is a change in the material properties of the boom at different temperatures, as seen from the shifts in the modes. State-space models were created for testing at two different temperatures using the vector-fitting approach. Estimation results and their corresponding errors were presented for each of the three axes at these temperatures. Although the results presented here were satisfactory, higher fidelity hybrid approaches such as the parametric Adaptive Anderson-Antoulas (pAAA) framework, which involves both least-squares fitting and interpolation, will be investigated in the future. A comparative study between the different system identification methods will need to be performed to find the best approach to solve this problem. These temperature dependent state-space models will be used to design active control experiments using piezoelectric patch actuators. This will demonstrate controllable deployment of self-deployable tape springs and minimize the deployment shock on the satellite chassis.

This data based model will help predict the system dynamics in the uncertain CubeSat environment (zero-g, cold, hot, vacuum of space). These models will be used to compare responses to the on-orbit data from the UPS-1 mission, helping to dynamically characterize this complex bistable deployable space structure.

Acknowledgments

We gratefully acknowledge the support from the Center for Space Science and Engineering Research at Virginia Tech (Space@VT) and VT Mechanical Engineering Department faculty Dr. Suyi Li. We would also like to thank NASA Langley Research Center, Drs. Juan M. Fernandez and Matthew Chamberlain, for providing the boom samples for testing and flight, and for consultations in designing the tests.

References

- [1] Betts, B. H., Spencer, D. A., Nye, B., Munakata, R., Bellardo, J., Wong, S. D., Diaz, A., Ridenoure, R. W., Plante, B. A., Foley, J. D., and Vaughn, J., “LightSail 2 : Controlled Solar Sailing Using a CubeSat,” 2016.
- [2] Whited, D., Angle, N., Engebretson, R., Gargioni, G., Gibbons, R. F., Kenyon, S., and Black, J., “Ut ProSat-1: A Platform for Testing Lightweight Deployable Composite Structures,” *36th Annual Small Satellite Conference*, 2023.
- [3] Engebretson, R. W., Du, M., Mhadgut, D., Rhodes, T., Spinetta, A., Gargioni, G., Whited, D., Davaria, S., and Black, J., “A Hybrid Deployer Mechanism for Active and Passive Deployment of a Parabolic Bistable Tapespring for Space Deployable Structures,” *ASCEND*, 2022, p. 4338.
- [4] Yao, Y., Ambruso, A., Fernandez, J. M., Bilén, S. G., and Ning, X., “A Multifunctional Bistable Ultrathin Composite Boom for In-Space Monitoring of Deployment Dynamics,” *SciTech*, 2023, pp. 1–10.
- [5] Mhadgut, D., Thomas, P., Du, M., Phoenix, A., Davaria, S., and Black, J., “Environmental Tests of a Parabolic Self-deployable Tapespring Boom for Cubesat Applications,” *SMASIS*, 2023.
- [6] Ewins, D., “Modal Testing - Theory and Practice (Mechanical engineering research studies)-Research Studies Pr,” 1984.
- [7] Maia, N. M. M., and Silva, J. M. M., “Theoretical and Experimental Modal Analysis,” , 1997.
- [8] Semlyen, A., “Rational Approximation oF Frequency Domain Responses by Vector Fitting,” *IEEE Transactions on Power Delivery*, Vol. 14, 1999.
- [9] Sanathanan, C., and Koerner, J., “Transfer function synthesis as a ratio of two complex polynomials,” *IEEE Transactions on Automatic Control*, Vol. 8, No. 1, 1963, pp. 56–58. <https://doi.org/10.1109/TAC.1963.1105517>.
- [10] Gustavsen, B., “Improving the pole relocating properties of vector fitting,” *IEEE Transactions on Power Delivery*, Vol. 21, 2006, pp. 1587–1592. <https://doi.org/10.1109/TPWRD.2005.860281>.
- [11] Deschrijver, D., Mrozowski, M., Dhaene, T., and Zutter, D. D., “Macromodeling of multiport systems using a fast implementation of the vector fitting method,” *IEEE Microwave and Wireless Components Letters*, Vol. 18, 2008, pp. 383–385. <https://doi.org/10.1109/LMWC.2008.922585>.
- [12] Le, S., “Active vibration control of a flexible beam.” 2009. <https://doi.org/10.31979/etd.r8xg-waar>, URL https://scholarworks.sjsu.edu/etd_theses/3983.
- [13] Adel, M., Ibrahim, K., Gad, A.-R., El, A., and Khalil, M., “Development of Dynamic Model for Vibration Control of Flexible Beam,” , 2016.
- [14] Aktas, K. G., and Esen, I., “State-Space Modeling and Active Vibration Control of Smart Flexible Cantilever Beam with the Use of Finite Element Method,” , 2020. URL www.etasr.com.
- [15] Li, C., Shen, L., Shao, J., and Fang, J., “Simulation and Experiment of Active Vibration Control Based on Flexible Piezoelectric MFC Composed of PZT and PI Layer,” *Polymers*, Vol. 15, 2023. <https://doi.org/10.3390/polym15081819>.
- [16] Drmač, Z., Gugercin, S., and Beattie, C., “Vector Fitting for Matrix-valued Rational Approximation,” *SIAM Journal on Scientific Computing*, Vol. 37, No. 5, 2015, pp. A2346–A2379. <https://doi.org/10.1137/15M1010774>, URL <https://doi.org/10.1137/15M1010774>.
- [17] Albakri, M. I., Malladi, V. V. S., Gugercin, S., and Tarazaga, P. A., “Estimating dispersion curves from Frequency Response Functions via Vector-Fitting,” *Mechanical Systems and Signal Processing*, Vol. 140, 2020. <https://doi.org/10.1016/j.ymssp.2019.106597>.
- [18] Malladi, V. V., Albakri, M. I., Krishnan, M., Gugercin, S., and Tarazaga, P. A., “Estimating experimental dispersion curves from steady-state frequency response measurements,” *Mechanical Systems and Signal Processing*, Vol. 164, 2022. <https://doi.org/10.1016/j.ymssp.2021.108218>.